

Manuscript title:

SpecSeg: cross spectral power-based segmentation of neurons and neurites in chronic calcium imaging datasets

Authors:

Leander de Kraker¹, Koen Seignette^{1*}, Premnath Thamizharasu^{1*}, Ildefonso Ferreira Pica¹, Christiaan N. Levelt^{1,2#}, and Chris van der Togt^{1#}

¹Netherlands Institute for Neurosciences, Molecular Visual Plasticity group, Meibergdreef 47, 1105 BA Amsterdam, the Netherlands.

²Department of Molecular and Cellular Neurobiology, Center for Neurogenomics and Cognitive Research, VU University Amsterdam, de Boelelaan 1085, 1081 HV, the Netherlands.

#Communicating authors

*Equal contribution

Contact Information:

Christiaan N. Levelt, Netherlands Institute for Neuroscience, Meibergdreef 47, 1013LM Amsterdam, the Netherlands. E-mail: c.levelt@nin.knaw.nl, Phone: +31-20-5665359

Chris van der Togt, Netherlands Institute for Neuroscience, Meibergdreef 47, 1013LM Amsterdam, the Netherlands. E-mail: c.van.der.togt@nin.knaw.nl, Phone: +31-20-5664698

Abstract

Imaging calcium signals in neurons of awake, behaving mice using two-photon microscopy makes it possible to study how learning alters coding in large neural populations. Such experiments produce extremely large datasets requiring powerful automated methods to extract responses from hundreds of neurons. Here we present a new open source toolbox for 1) segmentation of regions of interest (ROIs) representing neuronal structures, 2) inspection and manual splitting, addition or rejection of ROIs, 3) neuropil correction and signal extraction and 4) matching of ROIs in sequential recordings. Our toolbox is built around a novel method for the identification of ROIs based on temporal cross-correlations of low frequency components derived by Fourier analysis, of each pixel with its neighbors. The approach is insightful for the end user and allows for the ROI detection around neurons or irregular structures such as dendrites and axons by adjusting simple morphological constraints. This new pipeline thus provides an efficient and user-friendly approach for analyzing calcium responses in neuronal structures imaged over prolonged periods of time.

Keywords

Two-photon microscopy, calcium imaging, region of interest, automated, chronic, data analysis, ROI segmentation, cross-spectral power.

Introduction

The advances *in vivo* two-photon fluorescence microscopy (Engert and Bonhoeffer, 1999; Svoboda et al., 1996) and the development of genetically encoded fluorescent biosensors (Chen et al., 2013; Mank et al., 2008) have revolutionized neurobiological research over the last two decades. The combination of these techniques has enabled the imaging of neuronal activity in awake behaving animals over timespans up to many months. This provides combined anatomical and functional information at the cellular level for hundreds of neurons at the same time, or at the dendritic, axonal or synaptic level in more restricted numbers of neurons (Cichon and Gan, 2015; Gambino et al., 2014; Iacaruso et al., 2017; Jia et al., 2010; Petreanu et al., 2009; Szalay et al., 2016; Wilson et al., 2016; Winnubst et al., 2015). The insight this provides about the functions and interactions of specific neural subtypes in different brain regions of awake behaving animals was previously unthinkable.

The most used approach is the imaging of changes in intracellular calcium levels as a proxy for neuronal activity. This is achieved by making use of genetically encoded calcium sensors such as GCaMP6 (Chen et al., 2013), whose fluorescent properties change upon binding calcium. The mere size of the obtained datasets, which consist of movies of calcium-indicator fluorescence images, forms a considerable challenge for data analysis.

An important step in the analysis of calcium imaging data is the identification of cell bodies or neurites in the image sequences. Ideally, one can identify the same structures in recordings performed at different days over prolonged periods of time, allowing the assessment of changes in neuronal responses during learning at the single cell level. Identification of these regions of interest (ROI) is preferentially done in an automated fashion, as manual segmentation is neither reproducible nor scalable. Moreover, human annotators tend to include non-active ROIs and miss active ROIs with low background fluorescence (Giovannucci et al., 2019; Pachitariu et al., 2017). Automated ROI identification requires robust detection algorithms with minimal assumptions on the properties of ROIs to detect the circumferences of individual cells and neurites.

Various software packages have been published that accomplish this task, using different approaches. Cell boundaries may be detected by multiple coupled active contours (Reynolds et al., 2017). Matrix factorization approaches (Giovannucci et al., 2019; Maruyama et al., 2014; Mukamel et al., 2009; Petersen et al., 2018; Pnevmatikakis et al., 2016) determine the activity of neurons and their delineation by considering fluorescence as a spatiotemporal pattern that can be expressed as the product of a matrix encoding location and a matrix encoding time. Deep learning approaches (Apthorpe et al., 2016; Klibisz et al., 2017) define ROIs based on neuron features learned from data in which cells were manually detected. Dictionary learning approaches make use of neuron templates to identify ROIs (Pachitariu et al., 2017). Finally, correlation-based approaches define ROIs based on activity correlations between pixels (Kaifosh et al., 2014; Smith and Häusser, 2010; Spaen et al., 2019). All these approaches have their strengths and weaknesses. For example, deep learning approaches that select ROIs based on shapes must be trained for different types of data and may include neurons from which no signal can be extracted. Identifying ROIs with highly variable shapes is complicated for most approaches except those based on activity correlation. For most approaches it is often necessary to introduce significant adaptations to the software in order to make it suitable for specific experimental settings and the underlying calculations that define the ROIs can be difficult or impossible to track. In other approaches the outcome is significantly affected by initial parameters which are not self-evident and thus difficult to tweak. Correlation-based approaches are easy to understand and require few predefined constraints but can be severely limited by noise in the recordings. In this paper, we describe an open-source pipeline (Fig.1) for calcium imaging data analysis. It makes use of a novel approach for ROI detection, termed SpecSeg, which is based on cross-correlations of low frequency components, derived through Fourier transforms, of each pixel trace with its eight adjacent neighbors. It makes use of our finding that low-frequency fluctuations below 0.4 Hz are a signature of active neurons. Our approach is insensitive to noise, straightforward and highly insightful for the end user as it enables the visualization of the ROI detection process. It allows the detection of ROIs around irregular structures such as dendrites and axons and the

parameters set by the users are intuitive. The pipeline also includes a user interface for quality control and the manual splitting, addition or rejection of ROIs, and a tool to match ROIs in sequential imaging sessions (Fig. 1). Together, this new pipeline provides an efficient and user-friendly approach for analyzing calcium responses in neuronal structures imaged over prolonged periods of time.

Results

Pipeline

Figure 1 shows the components of our pipeline for the analysis of chronic calcium imaging datasets.

The pipeline requires motion-corrected calcium imaging data in raw TIFF or SBX (NeuroLabware) format. We use an adapted version of NormCorre (Pnevmatikakis and Giovannucci, 2017) to motion correct our SBX files. A motion corrected series of TIFF images can also be used, but this first needs to be converted to SBX format for which we provide a conversion tool.

The first step in the pipeline is ROI selection, which involves (a) the reorganization and downsampling of the data in order to speed up memory retrieval, (b) extraction of the frequency components of the fluorescence traces for each pixel (“pixel trace”) by Fourier analysis and the creation of images representing how well they correlate with those of neighboring pixels (c) the identification of peaks within the images and the construction of preliminary contours (ROIs), and (d) further refinement of the ROIs based on activity correlations within each contour. The second step in the pipeline is the ROI manager, a user interface for the inspection of the ROIs that has tools for manually rejecting, splitting or adding ROIs. The third step is neuropil subtraction and signal extraction and the final, fourth step is deconvolving the signals, using maximum likelihood spike estimation (MLSpike, Deneux et al., 2016).

In addition, a separate toolbox is included for matching the selected ROIs in sequential imaging sessions by aligning the images and measuring the overlap of ROIs between different sessions. The sensitivity of ROI matching can be changed easily with an overlap threshold and the results of the matching can be evaluated and edited. Below, each step in the pipeline is described in detail.

The MATLAB implementation of the toolbox and instructions on how to install and use the software can be found at <https://github.com/Leveltlab/SpectralSegmentation> .

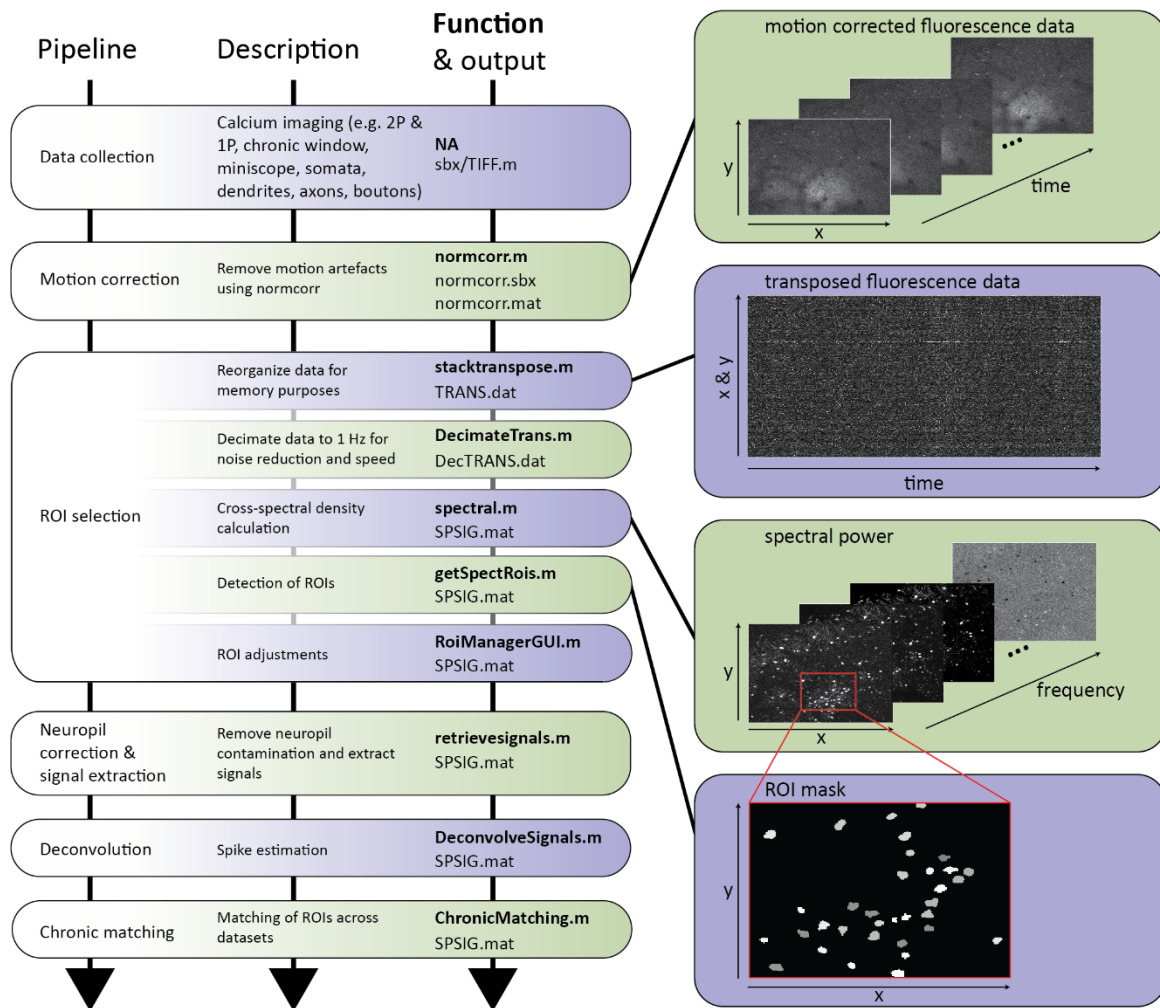


Figure 1. Overview of the pipeline for automated region of interest (ROI) selection and signal extraction.

Calcium imaging data needs to be motion corrected after collection using NoRMCorre. ROI selection involves data reorganization, extraction of frequency components of pixel traces and the drawing and refinement of ROIs around the peaks identified in the images based on the frequency components. A user interface allows for the manually rejecting, splitting or adding of ROIs. Next, neuropil is subtracted, and the signal extracted and deconvolved. A toolbox for matching of ROIs in repeated recordings is also provided.

ROI selection based on cross-spectral power

We established a novel approach for the automated segmentation of ROIs in calcium imaging data based on cross-spectral power of the pixel trace. To develop the method, we made use of calcium imaging data acquired repeatedly using two-photon microscopy in mice expressing the genetically encoded calcium indicator GCaMP6f in the primary visual cortex (V1) and tested it on a variety of different datasets from different brain regions and using different approaches.

The first step in the process (`stacktranspose.m`) is to transpose the image sequences to place time in the first dimension and width * height in the second dimension, and to downsample the data to approximately 1Hz (`DecimateTrans.m`), using the MATLAB `decimate` function (Mathworks®). This way, each pixel trace is organized in sequential order in memory and can be accessed rapidly, speeding up the next steps in the process.

Next is the cross-spectral power calculation (`spectral.m`). Each pixel trace is cut into overlapping one-minute segments, and a discrete Fourier transformation is applied to each segment to extract frequency components between 0.017 and 0.5Hz, with of bin width of 0.017Hz. Then we calculate the cross-spectral density function of each pixel with its 8 neighbors, and average these over all segments. Finally, the average cross-spectral density functions are normalized with the variances of each pixel and its neighbors, and the average cross-spectral power for each frequency component at each pixel is calculated (this estimate is a measure for how well pixels correlate with their direct neighbors at each frequency component). This results in a series of 30 images, each representing a different frequency component.

These images of spectral components provide a better basis for the selection of ROIs around active neurons than the fluorescent signal (Fig. 2A-B). We find that spectral components below 0.4Hz are the most indicative for active neural elements (Fig. 2C-I, Fig. 3A-C). As a consequence, when we compose images by translating the cross-spectral power of a particular low-frequency component into brightness, active elements in the image become very clearly separated from the background (Fig. 2C-F), even when their level of fluorescence is low (see neuron in red box). Interestingly, active

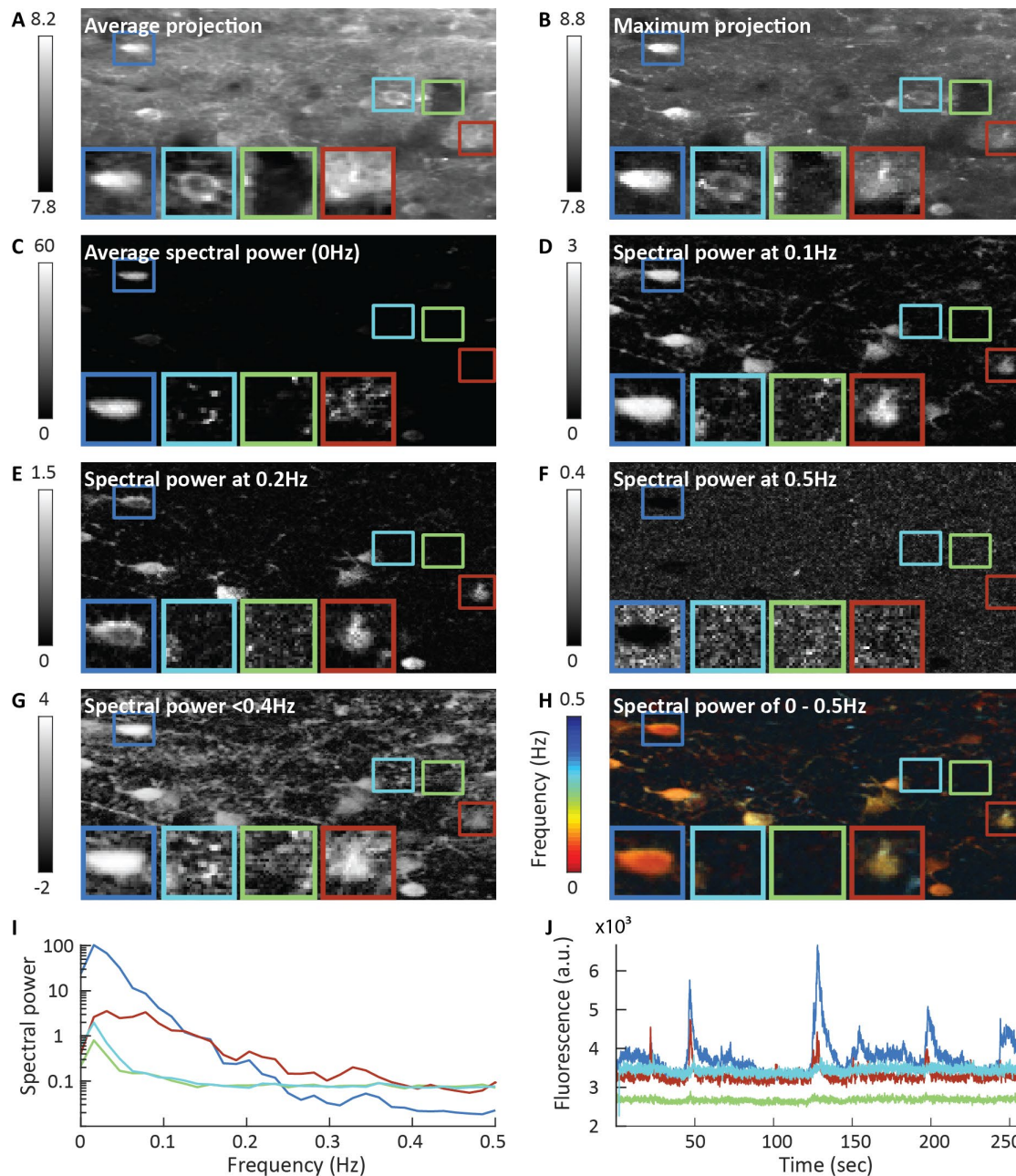


Figure 2. Comparison of fluorescence and spectral power images. **A)** Average fluorescence projection. The colored squares indicate regions containing an easily recognizable active neuron (dark blue); a silent neuron (cyan); no neuron (green); a hardly recognizable but active neuron (red). **B)** Maximum fluorescence projection. Note that the neuron in the cyan region can be easily detected, while the neuron in the red region is hardly visible. **C-H)** Cross-spectral images. Note that the silent neuron in the cyan region is hardly visible in the cross-spectral images, while the active cell in the red region can be easily identified. **I)** The cross spectral power of the four example areas. Note the logarithmic y-axis. **J)** Pixel traces of the example areas denoted in panel A-H.

neurons also look different in cross-spectral images. They no longer have a dark central nuclear region. Low frequency pixel correlations tend to show a central maximum that declines to the border of a neuron (Figs. 2, 3).

In contrast, non-active neurons with high levels of fluorescence, which are visible in the average fluorescence projection (Fig. 2A, J), do not show up in the spectral images (see neuron in cyan box). ROIs can thus be selected by searching for the largest local maxima in these spectral images and drawing contours around them (Fig. 3). Because the images of the different frequency components reveal different neurons and/or neuronal compartments, a complete set of ROIs is created by adding up all ROIs detected in the spectral images of all low-frequency components (Fig. 2G, H).

Automated ROI refinement

Some contours selected this way may still contain overlapping or closely juxtaposed neuronal elements (Fig. 3A-D), especially if the density of cell bodies or neurites is high. To prevent this problem, contours are further constrained based on whether the fluorescence pixel traces within the contour are tightly correlated as would be expected if they are from the same neuron. We do this by taking the median fluorescence trace of the pixel traces from the local maximum and its eight neighboring pixels and correlating this trace with each pixel trace in the preselected contour. This results in correlation values for every pixel in the ROI (pixel R). Next, using a threshold set at half the maximum correlation strength (this threshold can be adapted), a new contour is selected around the best-correlated pixels (Fig. 3E). To save an estimate of how well the fluorescence pixel traces are correlated inside an ROI, we square the pixel correlation values of an ROI and average them, resulting in the mean pixel R^2 (Fig. 3E). The mean pixel R^2 indicates how much of the pixel variance is explained by a shared signal within an ROI. We assume that this signal is the actual activity trace of a neuron, possibly including a general neuropil signal. The remaining variance is due to sources surrounding a neuron influencing individual pixel traces separately.

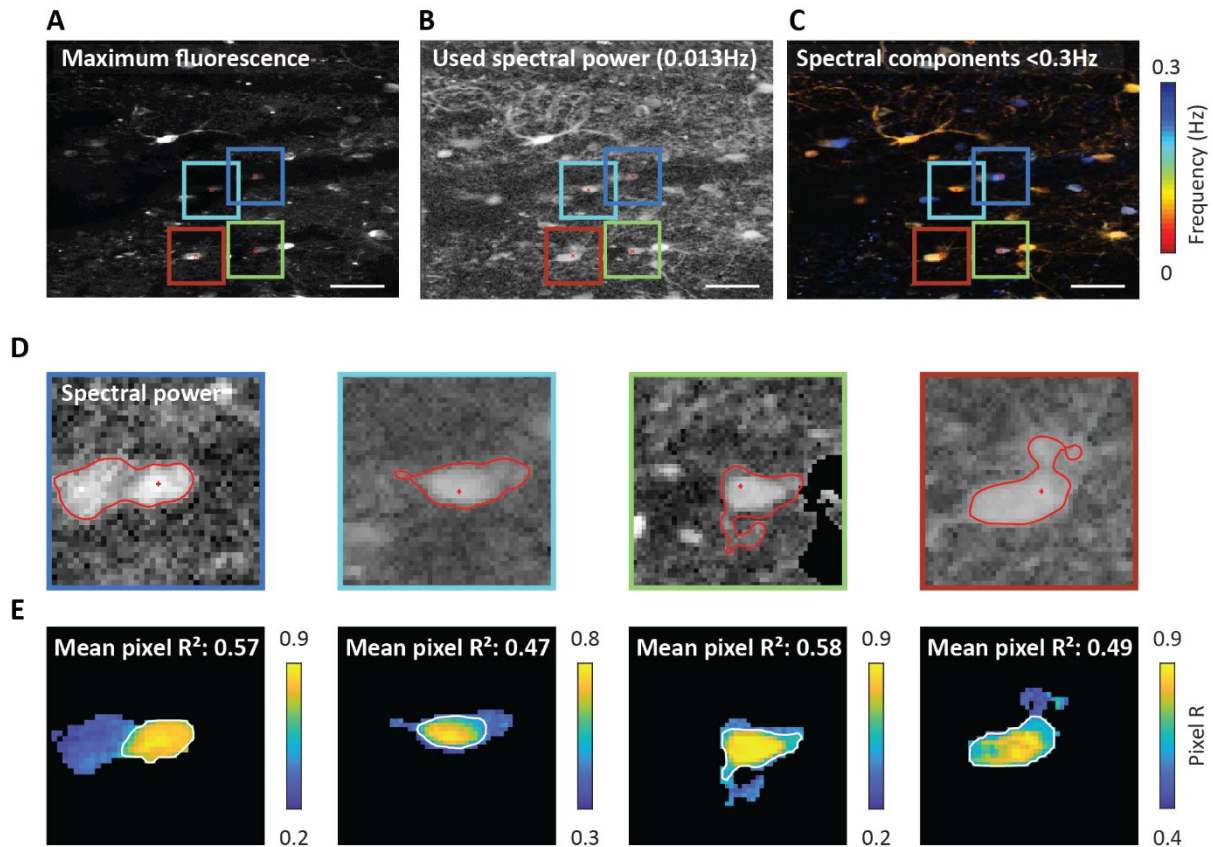


Figure 3. Automatic ROI creation and refinement. **A)** Maximum fluorescence projection of the recording. The colored squares denote four example areas that are selected for an ROI search based on local maxima of the cross-spectral image in the next panels. Scale bar = 40 μ m. **B)** The spectral power of the first frequency component (0.013 Hz) that is used in the ROI search. **C)** Cross-spectral power, with different frequency components displayed in different colors. **D)** The spectral power from panel B in the selected areas containing local maxima. The contour that is found around these putative neurons is displayed in red. For these neurons the threshold for pixel inclusion was too low, resulting in ROIs that are too large. These ROIs are automatically refined based on pixel correlation. **E)** The pixel correlations of the ROIs displayed in D. The color displays the pixel correlation of the signal from each pixel with the signal from the ROI local maximum. The pixel correlation threshold allows for ROI refinement. The new contour, shown in white, is determined by the pixel correlation values.

Versatility of ROI selection approach

Restrictions can be applied in order to select ROIs around cell bodies, such as the minimal and maximal surface area of the ROI or its roundedness. Without these restrictions, thin elongated contours can be easily selected, making it also possible to define ROIs on dendrites and axons (Fig. 4A-C). We tested the ROI selection approach on various datasets, including two-photon calcium imaging using a GRIN-lens in visual thalamus (Fig. 4D) and one-photon miniscope imaging in visual cortex (Fig. 4E). One-photon miniscope signals are generally more correlated and contaminated by out-of-focus signals. Spectral analyses therefore resulted in unclear separation of individual ROIs. A simple Gaussian background subtraction on the raw data strongly improved separation (Fig. 4E).

Comparison with other packages using Neurofinder

To compare the efficiency of our method with that of other packages that are available, we made use of Neurofinder datasets (<http://neurofinder.codeneuro.org/>). Our results (SegSpect0, by Spectral Segmentation) scored in the mid-range of all tested methods. Because this seemed a relatively low score considering the good results we obtained with SpecSeg on our own datasets, we looked at the Neurofinder results in more detail. We noticed that in several Neurofinder datasets, SpecSeg missed more than 50% of the Neurofinder “ground-truth” ROIs and found additional ROIs that were not included as ground-truth ROIs, both contributing to the lower score (Fig. 5A, D). To understand why SpecSeg selected different ROIs than those considered as ground truth, we calculated the mean pixel R^2 of the pixels within the latter ROIs (Fig. 5B, C, E, F) (see methods). This provides an estimate of how much of the pixel variance is derived from a shared signal within an ROI. When we sorted the ROIs based on the mean pixel R^2 , we noticed a sharp decline of this estimate in the ground-truth ROIs in all of the Neurofinder datasets (Fig. 5C, F). In the Neurofinder datasets, most ROIs had a mean pixel R^2 below 0.15, suggesting that > 85% of the signal variance in these ROIs originated from external sources or simply noise (Fig. 5G-H). ROIs selected by SpecSeg all had mean pixel R^2 values well above this level. This resulted in only part of the ROIs defined as

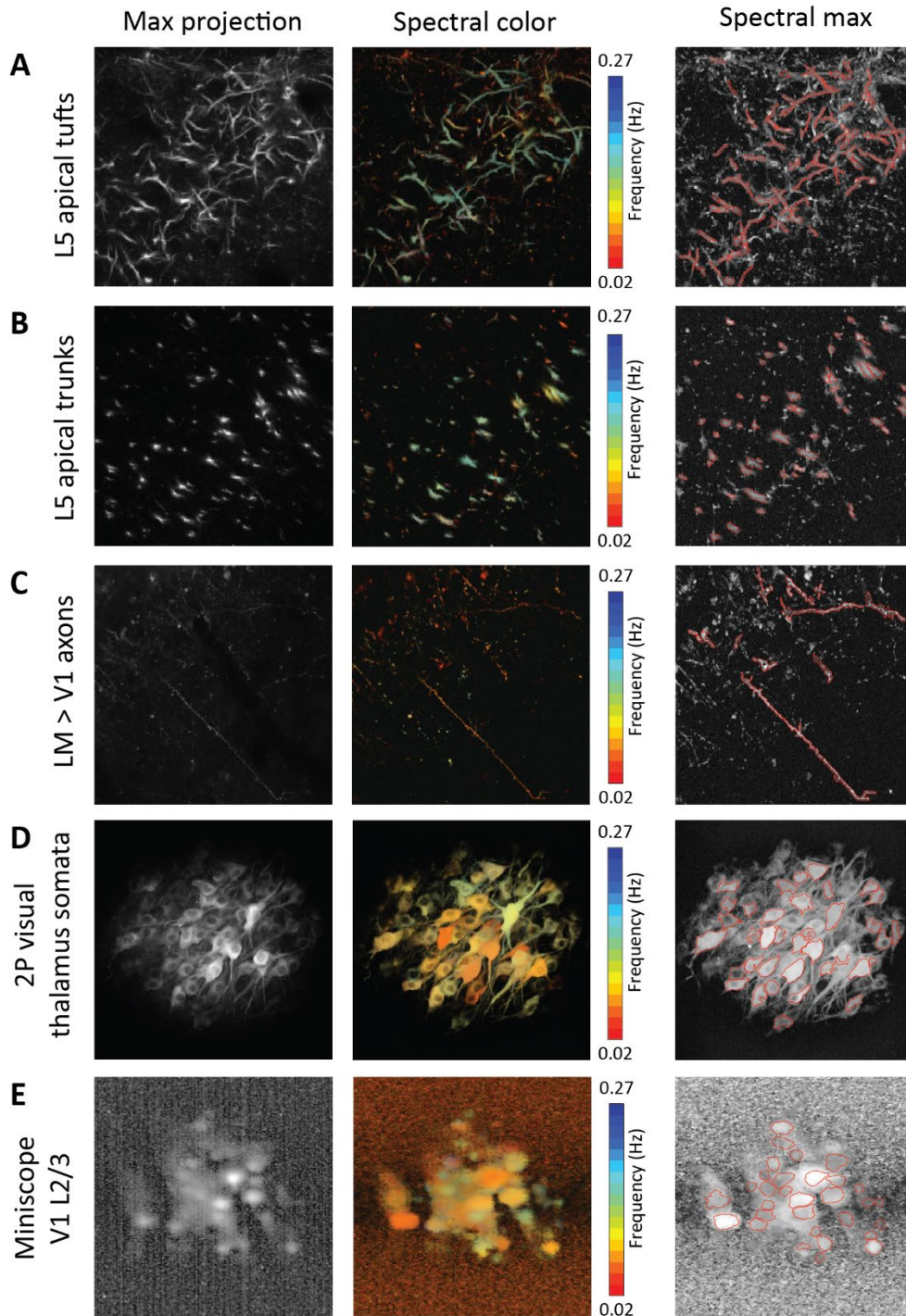


Figure 4. Examples of fluorescent signals, cross-spectral power and ROI selection in datasets derived from different brain regions and/or imaging techniques. Left column: maximum fluorescence projections. Middle column: cross-spectral power, with different frequency components in different colors. Right column: cross-spectral power maximum projection, with contours of ROIs in red. **A)** Two-photon microscopy of layer 5 apical tufts in mouse V1. **B)** Two-photon microscopy of layer 5 apical trunks in mouse V1. **C)** Two-photon microscopy of visual lateromedial area axon projections to V1. **D)** Two-photon microscopy of visual thalamus using a GRIN-lens. **E)** One-photon miniscope imaging in mouse V1 layer 2/3.

ground truth in the Neurofinder datasets to correspond with those drawn using SpecSeg.

Importantly, SpecSeg missed less than 1% of the ground-truth ROIs with a mean pixel R^2 over 0.3.

SegSpec also selected additional ROIs representing active neurons that were not identified among the Neurofinder ground-truth ROIs. These ROIs had high pixel correlations and showed clearly defined responses with high signal to noise ratios (Fig. 5A, D). This shows that it is crucial to select ROIs based on activity and not solely on cell morphology visualized by the baseline fluorescence of the calcium indicator, as some responsive neurons may be invisible especially when using calcium indicators with very low calcium-free fluorescence such as JCaMP7c (Dana et al., 2019).

Finally, we compared our ROIs with those obtained using Suite2P (Pachitariu et al., 2017). The authors of Suite2P define a model that combines the estimated signal of an ROI with its neuropil background. Using a cost function to minimize the difference between model and actual fluorescence time course, the parameters of this model for each pixel are estimated. To process the data in a timely fashion, the pixels traces were ordered in time and binned, limiting the amount of time points (<10000). This is similar to our implementation, however we decimate the signal, which gives slightly better results than binning. As with other tools using sophisticated mathematical approaches, the outcome can be dependent on initial assumptions that are not always clear and self-evident, e.g. in this case the parameter defining the temporal kernel should be equal for all cells, which may not be appropriate in various cases. As expected, we found overlapping subsets for ROIs with high mean pixel R^2 values. The ROIs that SpecSeg did not select generally had a mean fluorescence trace similar to the background fluorescence in the Suite2P visualization tool.

Together, we suspect that ground-truth ROIs in the Neurofinder dataset are largely based on anatomical characteristics of GCaMP6-expressing neurons and include many silent neurons. Hence, the best performing methods on the Neurofinder datasets may use convolutional neural networks trained on ground truths that include neurons with low pixel correlations. Whether neurons that show so little activity that they cannot be reliably separated from noise or neuropil activity should be included in the analysis is questionable, though.

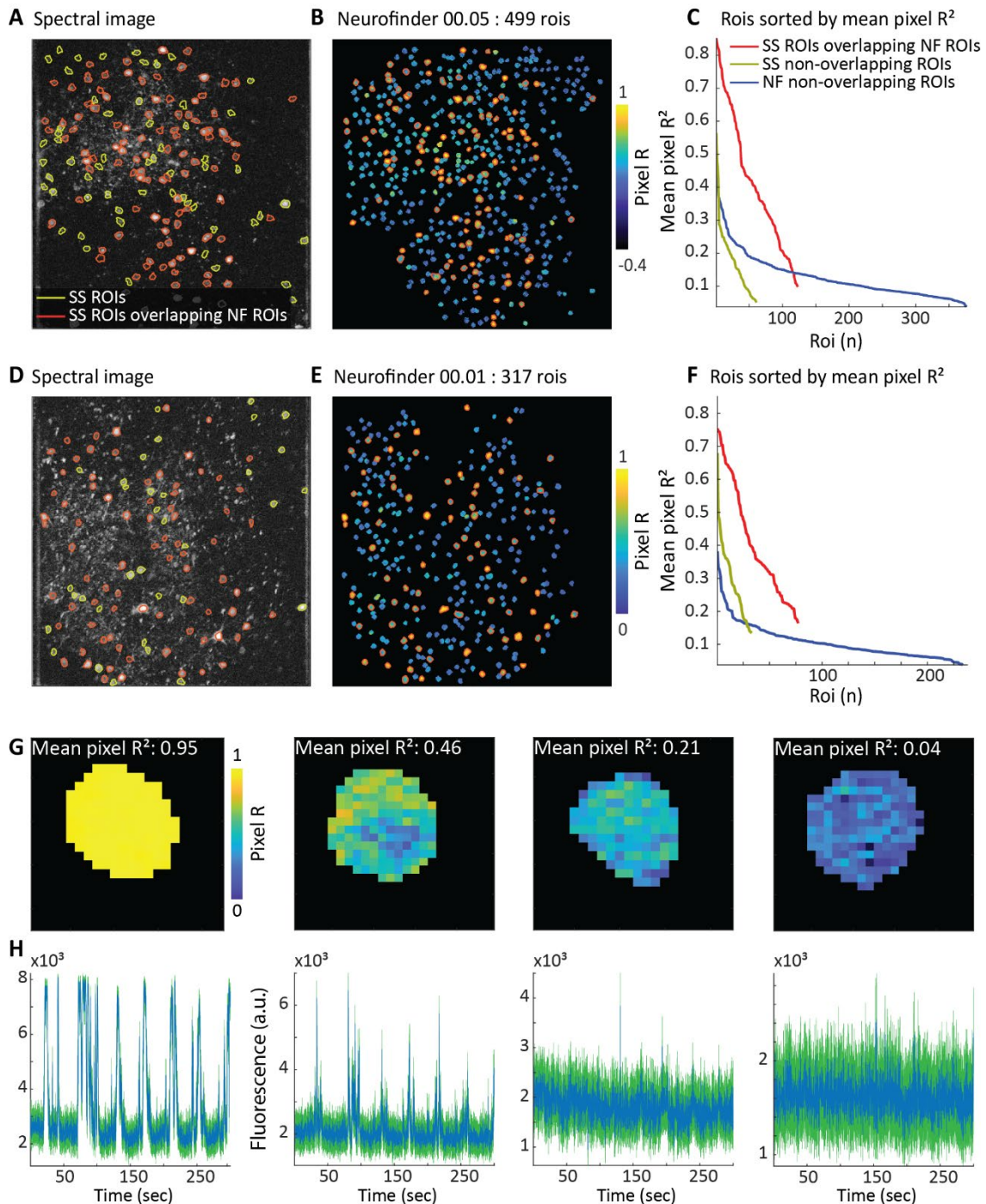


Figure 5. In Neurofinder datasets, SpecSeg (SS) only identifies ROIs from which a reliable signal can be extracted. A, D. Spectral images for the same datasets, with ROIs encircled by red (overlapping) and green (non-overlapping) contours. **B, E.** Pixel R for ground truth ROIs in Neurofinder (NF) datasets. Color bar indicates pixel R. Red encircled NF ground truth ROIs overlap with Spectral Segmentation (SS) ROIs. Note that SS has selected all ROIs with the highest mean pixel R^2 . **C, F.** Mean pixel R^2 of ROIs sorted by magnitude. NF ROIs overlapping with SS ROIs are plotted in red. The green line displays SS ROIs that do not overlap with NF ROIs, while blue line represents NF ROIs that do not overlap with SS ROIs. **G)** Correlation of each pixel trace within an ROI with the median pixel trace at the local maximum of cross-spectral power and its 8 neighboring pixels, of four example ROIs with decreasing mean pixel R^2 from the 03.00 NF dataset. **H)** Fluorescence traces (blue) plotted against their SEM * 3 (green) for the four example ROIs. Note that around a mean pixel R^2 of 0.2 or lower, the signal becomes non-significant.

Speed

In order to get an impression of the speed of our approach, we automatically timed the different components of the pipeline on two different computers analyzing 16 different datasets, varying in size from 6 to 51 gigabytes. Depending on the hardware that was used and the size of the dataset, the different components of the analysis pipeline varied in the time they required for completion (Fig. 6). This makes it difficult to provide hard numbers about the speed at which the SpecSeg pipeline processes the data. However, a useful indicator is that 1 hour of acquired data imaged at 15 Hz was processed by automated analysis in approximately 5 hours, from NoRMCorre motion correction until signal extraction. More than half of the time was used by the NoRMCorre motion correction. This illustrates that the speed of the SpecSeg pipeline is not a bottleneck, and in most cases performs the analysis overnight.

User interface for rejecting, splitting or manually defining ROIs

The automated procedure for selecting ROIs is highly effective. However, in some cases, ROIs can still be found that contain signals from multiple neurons or do not seem to represent a neuronal structure. Because such errors can cause misinterpretation of calcium imaging data, we developed a graphical user interface for splitting or deleting such ROIs. Additionally, because the automated ROI selection process is activity dependent, ROIs are not drawn around neurons that are not active in the imaging session. The user interface also allows adding ROIs for such neurons (Fig. 7A), in case the experimenter wants to include them in their analysis – for example in a chronic experiment in which the neurons do show activity in other recording sessions.

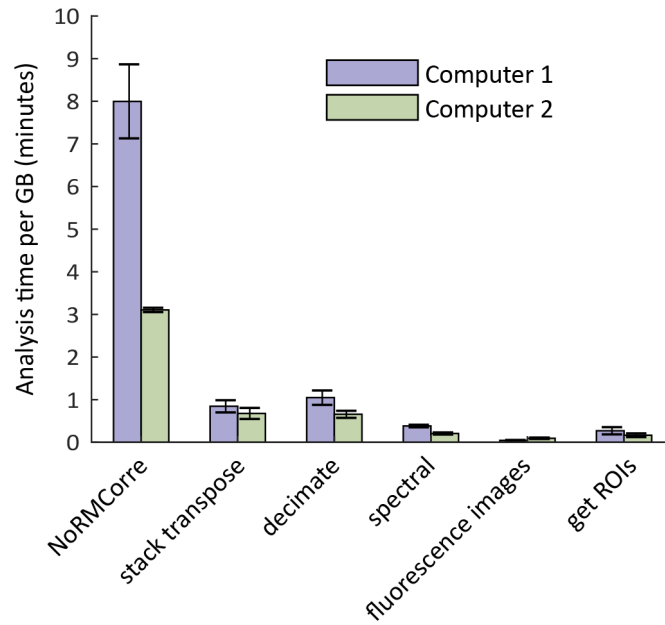


Figure 6. Timing analysis pipeline. Timing the analysis per GB of raw data with two different computer systems. Computer 1: 2x CPU: intel xeon E5-2620 2.4GHz, 6 cores. RAM: 96GB. Computer 2: CPU: intel core i7-4770 3.4GHz quadcore. RAM: 32GB. Total automated analysis time including motion correction with NoRMCorre. Computer 1: 10.6 minutes per GB (n=8). Computer 2: 4.5 minutes per GB (n=8). Not including NoRMCorre. Computer 1: 2.5 minutes per GB (n=8). Computer 2: 1.8 minutes per GB (n=8). Error bars shows the standard error of the mean.

Sometimes ROIs are created that envelop multiple neurons (Fig. 7B). To visually guide the splitting of these ROIs, pixel traces within the ROI are correlated with four reference points and correlation values are color coded. In case the ROI contains signals from more than one neuron, this becomes clearly visible (Fig. 7C). The correlation values are then used in k-means clustering to split the ROI into multiple ROIs, or to delete parts of the ROI, on the user's request (Fig. 7D). ROIs can also be deleted entirely or marked to be kept when more stringent criteria for ROI selection are applied. Finally, ROIs can be drawn in manually, or added by the computer, based on the fluorescence or spectral image (Fig. 7A). Altogether, these additional tools provide the means to adjust the ROI selection process in an easy and user-friendly way.

Neuropil correction and signal extraction

Once the ROIs are selected, the calcium signals from the cells can be extracted by averaging all pixel traces within the ROI contours. However, because the calcium signals from the neuropil can contaminate those of the cells, neuropil signal is first subtracted from the ROIs (Zhou et al., 2018). To achieve this, we select an area surrounding each ROI, taking care to avoid other ROIs (Fig. 8, see methods for details). The average of the pixel traces in this area is used as an estimate of the local neuropil activity. After multiplying it by 0.7 it is subtracted from the averaged fluorescence trace from the selected ROI. This method of neuropil subtraction is widely used (Chen et al., 2013; Khan et al., 2018; Tegtmeier et al., 2018).

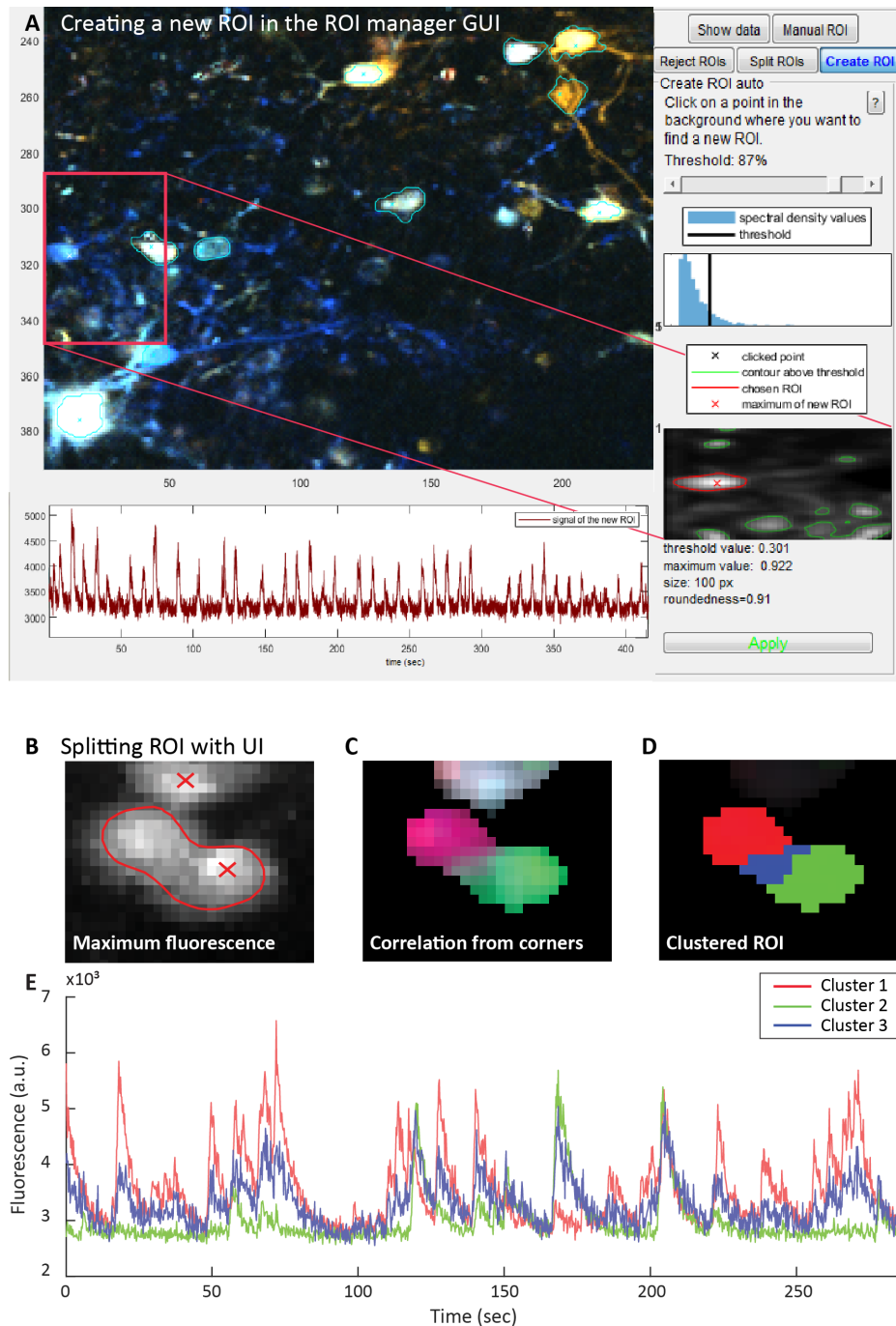


Figure 7. ROI manager user interface. **A)** A screenshot of the user interface. The functionality is set to ROI creation. The ROI creation function of the UI allows the user to add additional ROIs based on the current image in the UI. The current image shown in A is the cross-spectral power, in which several frequencies are shown in different colors. **B)** Maximum fluorescence of a ROI that envelopes two neurons. **C)** To guide and calculate the ROI splitting the fluorescence signal from the four corners is correlated with the all fluorescence pixel traces in the ROI. This results in four correlation values per pixel, which are shown in different colors. **D)** The ROI is clustered into three clusters with k-means clustering using the correlation values from C. The number of clusters is set by the user. **E)** The fluorescence signal of the three clusters.

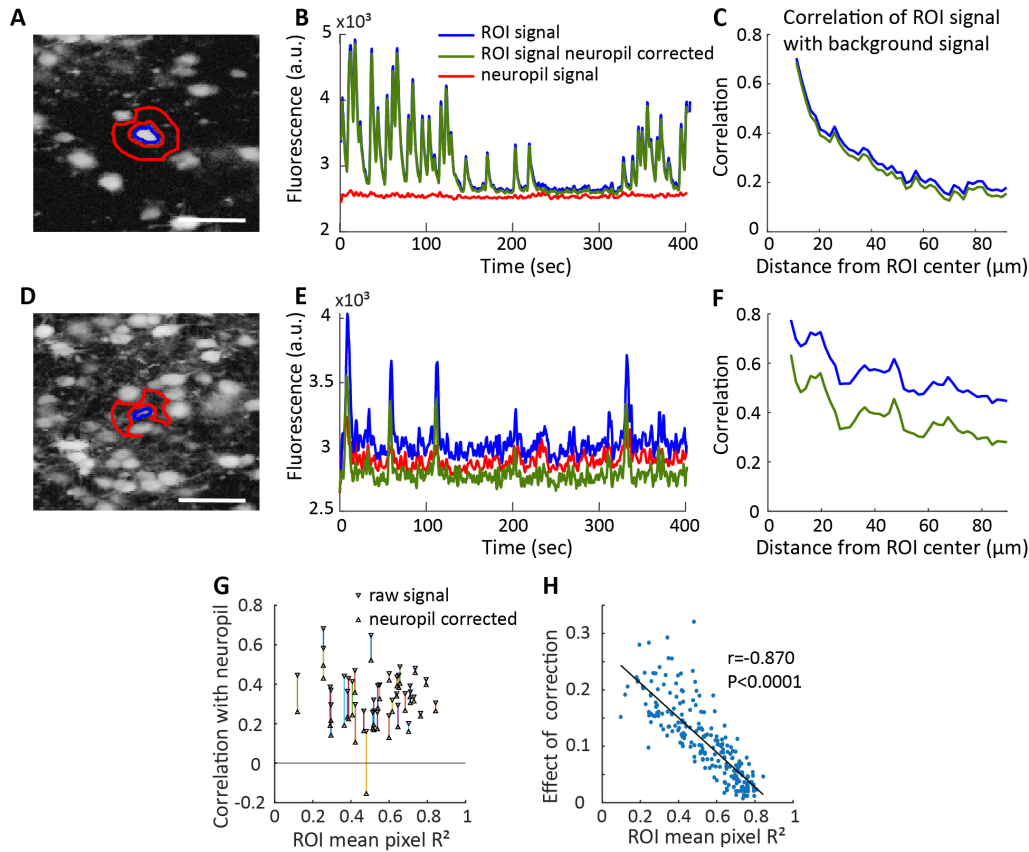


Figure 8. Neuropil estimation from surrounding pixels. **A, D**) Spectral image with an example ROI (blue contour) and surrounding background (red contour). **B**) Fluorescence signal of the example ROI of **A**. The neuropil signal is almost non-existent and neuropil correction does not change the ROIs' signal much. **C**) Correlation of neuropil signal with ROI signal depends on the distance from the ROI. The fluorescence signal was extracted from rings at increasing distances around the example ROI, excluding other ROIs. Those background signals were correlated with both the raw signal of the ROI (blue line), and with the ROIs' neuropil corrected signal (green line). Neuropil correction slightly decreases the correlation of the background signal. **E**) In this ROI the neuropil signal caused more contamination than in the example of **A**. Neuropil signal was larger because more dendrites are present, and the ROI itself has a less strong signal. The neuropil correction seems necessary for this ROI. **F**) The neuropil correction decreases the correlation with the surrounding background signal. **G**) Correlation with neuropil signal of multiple ROIs, before and after neuropil correction. The distance between these shows the 'neuropil correction effect'. **H**) The neuropil correction effect is significantly smaller when an ROI has a stronger mean pixel R^2 .

To test how our neuropil subtraction alters the signal, we correlated the pixel trace of ROIs with the pixel traces from the surrounding area (Fig. 8A-F). We found that in our data, neuropil correction barely changes the ROI signal in most cases (Fig. 8A-C). In some cases, however, the signal improves after neuropil subtraction (Fig. 8D-F). There may be multiple reasons why neuropil subtraction has less effect in our hands than in studies by others (Pachitariu et al., 2017). Experimental conditions such as the number of neurons that are labeled, the brain region that is imaged or the calcium indicator that is used will influence to what extent neuropil contaminates the signal (Pachitariu et al., 2017). An additional possibility is that when ROIs with a high mean pixel R^2 are selected, those ROIs that have a weak signal and are strongly influenced by neuropil are excluded. To test this directly, we plotted the effect of neuropil correction on the signal extracted from ROIs against their mean R^2 (Fig. 8G, H). This revealed that indeed, ROIs with higher mean pixel R^2 are barely affected by neuropil correction while those with low mean pixel R^2 are strongly affected. Thus, selection of ROIs with high mean pixel R^2 has the added advantage that it reduces the need for neuropil subtraction.

Automated retrieval of the same ROIs in chronically recorded datasets

One of the great strengths of two-photon microscopy of calcium responses in neuronal cell populations is that changes in neuronal activity can be followed at the single cell level over prolonged periods of time. To achieve this, it is essential to identify the same ROIs in chronic recordings of the same brain region. In very large datasets containing many recordings, this is a daunting task to do by hand, even after automated ROI selection. We therefore developed a toolbox for automated matching of ROIs in chronically recorded datasets. It involves the registration of the sequential recordings with each other, through translation and rotation of the spectral images. Next, overlapping ROIs are searched for in all possible pairs of recordings in the series (i.e. each recording is compared to all other recordings). By thresholding for a minimal amount of overlap between each pair of ROIs in both directions, only ROIs with similar shapes and sizes are matched. Finally, merging

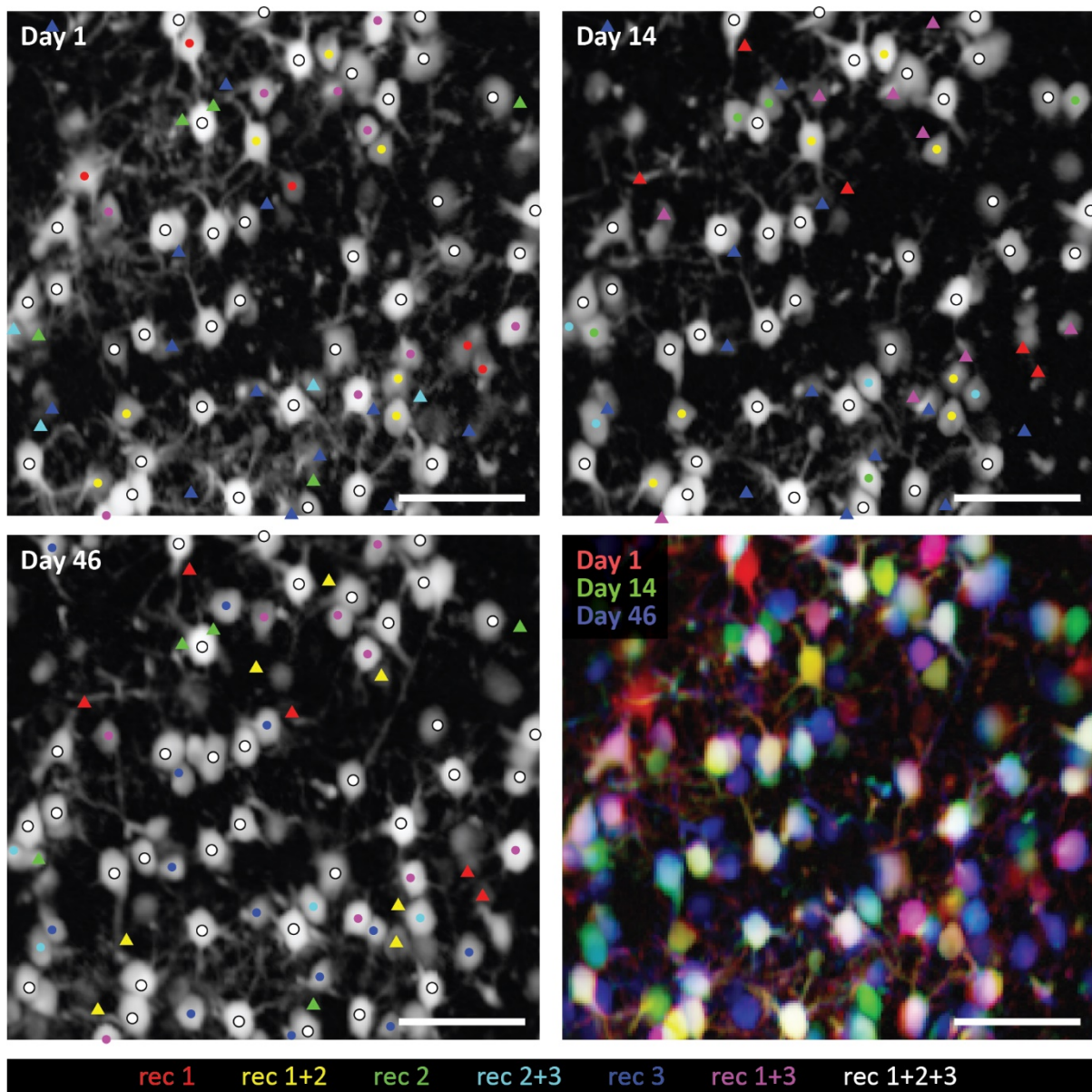


Figure 9. An example of matched ROIs in three sequential recordings. An ROIs center of mass (CoM) is shown with a dot. The dot's color shows in which recordings ('rec') it was found back. The triangles denote the position of some CoMs of ROIs that were present in other recordings, but missed in the recording in which the triangle is shown. The color denotes in which recording the ROI was present. The right bottom figure shows the three spectral images overlaid with red, green and blue colors, resulting in the same color mixing as the ROI CoM dots. Scale bar: 40 μ m.

all the matched pairs of ROIs results in a “matching matrix” containing the matched ROIs that are found in the series of recordings.

An example of ROI matching in three sequential recordings of V1 neurons, performed with 2-4 weeks in between sessions, is shown in Fig. 9. In these color-coded images, many cells can be retrieved in all three recordings. However, some neurons are not retrieved in one or two of the recordings, as indicated by the triangles. This may be caused by various factors, such as the precise angle and depth of the recording, changes in viral expression of the calcium indicator or the lack of activity of a neuron during one of the recordings.

Comparing ROIs between recordings

For a quantitative assessment of the number of ROIs that can be matched between recording sessions we analyzed data from 5 mice that were imaged 7, 8, 12, 13 and 12 times respectively, over a period of 2-5 months. This resulted in 21, 28, 66, 78 and 66 possible pairs of recordings respectively, in which we investigated the number of matched ROIs. With all data of the five mice pooled together, $37.7\% \pm 21.3\%$ of the ROIs were matched between recordings pairs, corresponding to 94 ± 57 ROIs. The percentage of matched ROIs was calculated as the percentage of matched ROIs in the recording with the least ROIs per recording-pair.

The number of matches was influenced by the time between two recordings. Fig. 10A shows that there was a significant correlation between the number of matched neurons and the time between recordings in two of the three mice (Spearman correlation, for mice 1 and 2 $P < 0.005$, for mice 3, 4 and 5 $P < 0.0005$, $r = -0.6, -0.35, -0.66, -0.93, -0.68$ for mice 1 to 5 respectively. The fits shown in the figure are exponential fits ($y = a * e^{b * x}$) with the initial value (a) at 75, 71, 53, 56, 61(%), and decay rate (b) at $-0.0084, -0.0036, -0.0171, -0.0160, -0.0123$ for mice 1 to 5 respectively). This suggests that it is not only variations in the angle or exact location of the recordings that determines whether ROIs can be matched, but probably also slower, biological processes such as viral expression of the calcium indicator, learning- or age-induced changes in neural activity, cell death or anatomical

changes of the brain. Indeed, Fig. 10B shows that correlations between the registered spectral images decreases over time (spearman correlation $P=0.0006$ for mice 1, for all other mice $P<0.0005$, $r=-0.68, -0.58, -0.61, -0.93, -0.82$ for mice 1 to 5 respectively), suggesting that the structure of the imaged location and activity patterns and GCaMP6f labeling of the neurons alter over a period of weeks to months. Changes in GCaMP6f labeling and/or neuronal activity is supported by the observation that more ROIs were detected on later imaging sessions for some mice (spearman correlation $P=0.2, P=0.008, P=0.51, P=0.97, P=0.015$, and $r=0.56, 0.83, -0.21, -0.01, 0.68$ for mice 1 to 5 respectively) (Fig. 10D). Finally, we tested what fraction of ROIs could be tracked in multiple sessions. For pooling the data from the 5 imaged mice, we were constrained by the minimum number of recordings of the mice. We therefore limited the number of sessions to 7, choosing the sessions in such a way that the number of days between the first and last recording was close to 65. We then calculated in how many imaging sessions the ROIs from recording 1 were found back in subsequent sessions (Fig. 10C). If ROIs were found in 6 or less sessions, this was not necessarily in consecutive ones. As shown in figure 9, ROIs can be missing for some sessions, and then show up again. We found that 22% of all ROIs could be matched in all 7 recordings, averaged over the five mice, which corresponded to 213 neurons, or $213*7=1491$ separate ROIs in total. 28% of ROIs (354 ROIs) could not be matched with ROIs from any other recording. Together, these results show that the developed pipeline is highly efficient in identifying ROIs and tracking them over many imaging sessions with little effort of the user.

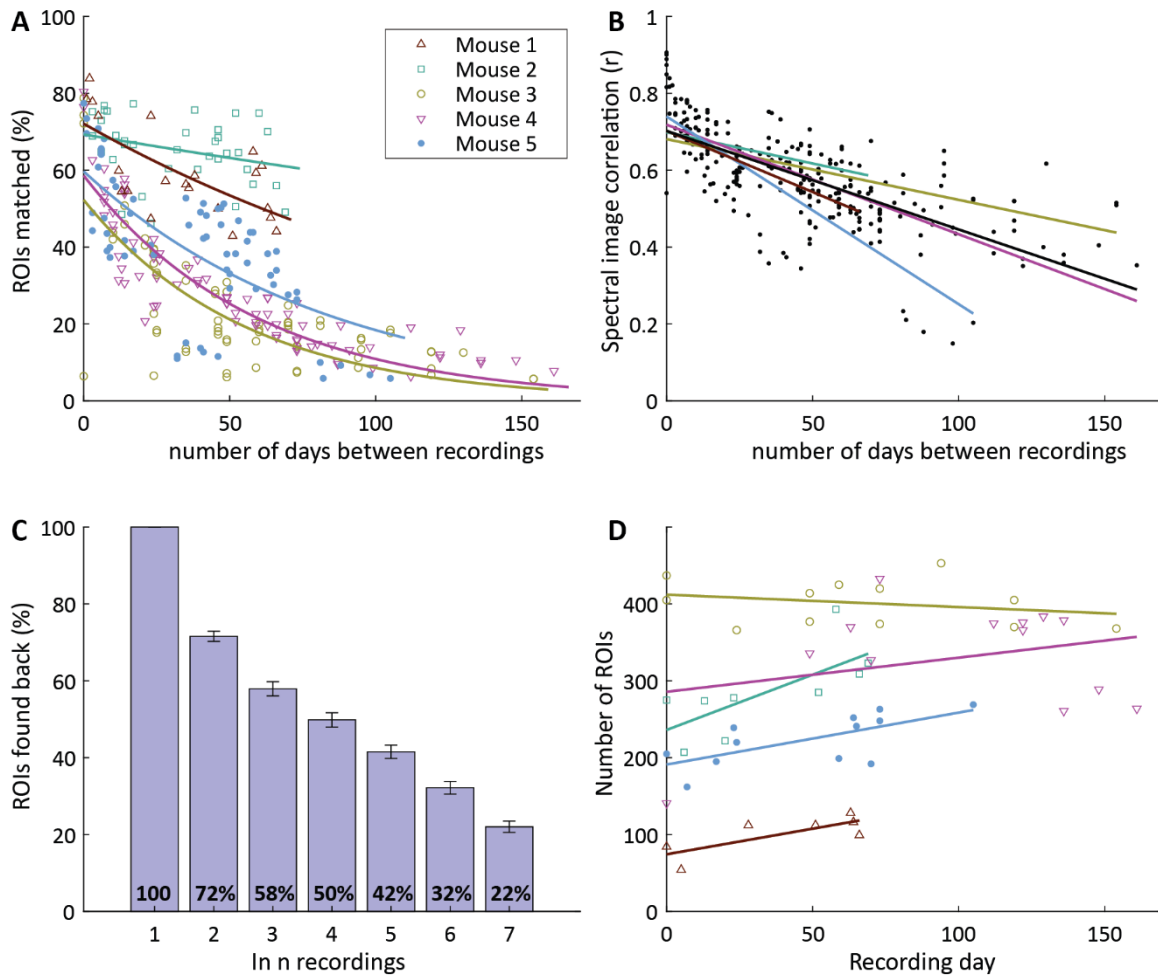


Figure 10. Chronic tracking. **A)** The number of matches between recordings decreases if there is more time between the recording pairs. **B)** Spectral correlation for each recording pair. Recordings that are recorded closer together in time have better correlation coefficients. This shows that the imaged brain changes over time. **C)** Checking in how many recordings the ROIs from recording one were found back in all seven recordings. To be able to pool all the mice together seven recordings were analyzed per mouse. Recordings were chosen so that the time between the first and last recording was as close to 65 days as possible. The number of putative neurons in each condition were: 1146, 792, 606, 516, 421, 319 and 213 for conditions 1 to 7 respectively. Error bar shows standard error of the mean for the five mice. **D)** The number of ROIs found in the mice recordings did increase significantly for mouse 2 and 5 (spearman correlation: $P < 0.05$, for mouse 1, 3 and 4 the P values were 0.20, 0.51 and 0.97 respectively).

Discussion

Here we describe a novel open source toolbox for automatic ROI selection, ROI editing, neuropil correction, signal extraction and chronic matching of ROIs. Our ROI selection is based on clustering of co-active pixel traces combined with morphological filtering to identify somata and neurites alike. Pixel correlations were also used in several other approaches for ROI selection (Kaifosh et al., 2014; Smith and Häusser, 2010; Spaen et al., 2019). In our implementation, however, the first step of ROI selection involves calculating the low (0.013-0.5Hz) frequency cross-spectral power components. These spectral components can be visualized, yielding exceptionally clear images of the local functional anatomy that include neuronal cell bodies and neurites. Underlying these low-frequency components are bouts of neuronal activity, which cause a prolonged rise in the fluorescence of the calcium indicator. In contrast to the high-frequency components, the low-frequency components are less sensitive to noise. Moreover, neuropil shows little low-frequency activity thus allowing for the efficient separation of neuronal structures from the background.

This first step of our ROI selection process requires only few initial constraints, allowing inclusion of ROIs with irregular shapes or sizes. During the second step, a threshold is set on the pixel correlations within the ROI, which leads to a robust separation of ROIs containing highly correlated pixels and rejection of areas of pixels in overlapping neural elements. Additional filters for morphological properties of the ROIs such as size or roundedness can be included. Adjustment of these constraints makes it possible to select ROIs around neuronal cell bodies, dendrites or axons. These constraints are intuitive and easy to use, making the SpecSeg ROI selection process very versatile and user friendly.

The pipeline also includes a graphical user interface, facilitating quality control of the selected ROIs. This interface comprises an alternative method for visualizing pixel correlations within the ROI, aimed at detecting whether multiple cells are present within one ROI. This makes it easy to split or reject ROIs if necessary. Also, ROIs can be added if the experimenter believes that cells are missed, and the quality of their signal can be assessed immediately.

We used the NeuroFinder datasets (<http://neurofinder.codeneuro.org/>) to compare the efficiency of the automated ROI selection procedure with other ROI segmentation packages available. This revealed that SpecSeg scored lower than other frequently used packages such as Suite2P (Pachitariu et al., 2017) and CalmAn (Giovannucci et al., 2019). This could be caused by the settings we used for ROI selection, by limitations of our ROI selection approach, or by what are considered “ground-truth” ROIs in the Neurofinder datasets (or a combination of these factors).

When we performed quality control on the Neurofinder ground-truth ROIs, we noticed that in a considerable subset the pixel traces within the ROI showed very little correlation. This implies that most of the signal extracted from pixels in such ROIs does not represent the signal from the ROI itself, but rather from surrounding neuropil. In contrast, SpecSeg only included ROIs with a high signal to noise (SNR) ratio. This also included ROIs that were too dark to detect by assessing the average fluorescent signal alone and were missed in the Neurofinder ground-truth ROIs. This means that SpecSeg selects the most relevant ROIs but misses ROIs of neurons that are silent during the recording. A similar observation was made in a study comparing ROIs identified automatically using CalmAn and those identified by human annotators. It was found that matching ROIs were preferably those with a high SNR (Giovannucci et al., 2019). To achieve a more refined set of ROIs, that more closely match ROIs selected by human annotators, both CalmAn and Suite2P include a final step to exclude spurious ROIs by training classifiers (Giovannucci et al., 2019; Pachitariu et al., 2017).

In SpecSeg, we chose to rely as little as possible on human annotation (directly, or indirectly by using trained classifiers) because our analyses revealed that this results in the inclusion of many ROIs with low SNR. We think it is debatable whether such ROIs should be included in the data analysis, as they may contaminate the actual neural code of the imaged neurons. When electrophysiological approaches are used, units with a signal that cannot be reliably separated from background noise would certainly not be included in the analysis. Only in some instances it is useful to know that a neuron is included in the dataset but does not show any activity, for example when chronically tracking the activity of individual neurons. In such cases, the option to manually include neurons

using the SpecSeg graphical interface when they are not detected by the activity-based approach can solve the issue. An additional problem with using trained classifiers is that they will need to be retrained when other structures than neuronal cell bodies need to be identified for ROI selection, such as axons or dendrites.

We included a neuropil subtraction approach in our pipeline that works similarly to previously described methods (Chen et al., 2013; Khan et al., 2018; Tegtmeier et al., 2018). It calculates the signal from a donut-shaped area around the ROI, which is then subtracted from the signal derived from the ROI. We noticed that for most ROIs, neuropil correction did not significantly improve the neuronal signal. Of course, the level of neuropil contamination depends on many factors, including the brain region imaged, the strength of the neuronal signals, the density of labeling and the synchronicity of neuronal activity. After more thorough analysis, we noticed that ROIs with high mean pixel R^2 were much less contaminated by the neuropil signal than those with low mean pixel R^2 . It should be noted that in ROIs with low mean pixel R^2 , neuropil subtraction may actually introduce an artefact in the signal, again illustrating the importance of removing such ROIs from the analysis.

It is difficult to compare the speed of the ROI selection process to other software packages available. However, we found that motion correction using NoRMCorre was the slowest step in the process, taking up approximately half the time of the total automated ROI selection process. This implies that the actual ROI selection process is not a bottleneck. Importantly, we found that the speed of ROI selection was more than sufficient for all practical purposes except on-line ROI selection.

One of the strengths of calcium imaging approaches is that one can follow the responses of individual neurons over prolonged periods of time. To facilitate this approach, we developed a tool for automated matching of ROIs in whole series of sequentially recorded calcium imaging sessions. Using this approach, about half of the ROIs between two randomly selected pairs of recordings could be matched. As already mentioned, one cause for not retrieving ROIs in all recordings is that some neurons are silent during some recordings, and thus not included by our activity-dependent ROI

selection approach. Also, ROIs may be missed due to slight misalignments of the imaged brain region. Interestingly, we found that when the time between two recordings was longer, the number of matched ROIs was reduced. This shows that biological factors also play a role in the success rate by which neurons are detected in multiple recordings. Over time, the brain may slightly change its shape, causing some neurons to be excluded from the field of view. Moreover, neurons may die, or lose or gain expression of the viral vector. The most interesting reason seems to be that neurons may not be active in some recordings, in line with the finding that when mice perform the same task over prolonged periods of time, neuronal activity patterns reorganize over time resulting in the recruitment of different sets of neurons (Driscoll et al., 2017). Together, these issues may explain why studies in which the chronic tracking of activity of individual neurons are still sparse. Our automated matching approach will make this exciting possibility of two-photon calcium imaging more accessible.

In conclusion, SpecSeg is a powerful, complete and open-source pipeline for ROI selection, signal extraction and chronic ROI matching that can be used on a variety of 1P and 2P calcium imaging data. Its main advantage over several existing calcium imaging toolboxes are the ease of use and simplicity, the intuitive way ROIs are selected and constrained, the selection of ROIs that represent neurons whose responses can be well separated from background noise, the possibility to select ROIs of various shapes and sizes, and its graphical interface for ROI editing.

Materials and methods

Mouse experiments

To develop the ROI selection tools described in this study, we made use of two-photon imaging data from mice that were repeatedly imaged in as yet unpublished behavioral studies. Here we describe the methodology developed for the analysis of such data. All animal experiments were approved by the institutional animal care and use committees of the Royal Netherlands Academy of Arts and Sciences. We used male and female mice that were 2-7 months of age. The mice were offspring of Ai14 mice (Cre-dependent tdTomato reporter mice, strain 007908) crossed with mice expressing Cre in vasoactive intestinal polypeptide (VIP)-expressing or somatostatin (SOM)-expressing interneurons (Jackson Laboratories, www.jaxmice.jax.org, strains_010908 and 013044 respectively). All animals were kept in a 12 h reverse day/night cycle with access to food and water ad libitum. Experiments were carried out during the dark cycle.

Viral injections

Mice were injected with a viral vector driving expression of the genetically encoded calcium sensor GCaMP6f in neurons (AAV2/9.syn.GCaMP6f, UPenn Vector Core facility). Anesthesia was induced with 5% isoflurane and maintained at 1.6% isoflurane in Oxygen (0.8L/min flow rate). Mice were administered Metacam (1mg/kg subcutaneously (s.c.), for analgesia) and dexamethasone (8 mg/kg s.c.) to prevent cerebral edema/inflammation and Cefotaxim (25 mg/kg s.c.) as antibiotic prophylaxis, after induction of anesthesia. Mice were head-fixed on a stereotax, scalp and soft tissue overlying the visual cortex were incised and the skull exposed. A small hole was drilled in the skull overlying the center of primary visual cortex (V1). A pulled capillary with AAV2/9.syn.GCaMP6f was inserted vertically through this hole to a depth of 200-400 um from the brain surface. Approximately 20 to 100 nl of virus (titer $\sim 10^{12}$ viral genomes per ml) was injected slowly using a Nanoject and the hole was covered with bone wax. During the surgery, the temperature was maintained with euthermic

pads. Respiration was monitored to adjust depth of anesthesia. Eyes were protected from light and from drying using Cavasan eye ointment. Once the window was made the exposed dura was continuously kept moist with artificial aCSF, consisting of a solution of 125 NaCl, 10 Hepes, 5 KCl, 2 MgSO₄, 2 CaCl₂, and 10 Glucose, in mM. Later the scalp was sutured, and the animal allowed to recover from anesthesia.

Cranial Window Surgery

One month after viral vector injection, mice were anesthetized again as described above. Mice were head-fixed on a stereotax and scalp and soft tissue overlying the visual cortex were incised and the skull exposed. A metal ring (5mm inner diameter) was fixed on the skull centered on V1, with dental cement. A cranial window was made inside the ring and the dura was exposed. The cranial window was then covered with a double coverslip (to reduce brain movements under the microscope) and fixed to the metal ring using dental cement. Animals were allowed to recover after the dental cement dried. After a minimum of 2 weeks of recovery, mice were submitted to further handling and training. During the training and recording periods described below, animals were typically in the setup 5 days per week.

Handling and habituation

Once an animal recovered from the viral injection, and before window implantation, animals were handled daily for 5 minutes (or until they started to groom while being handheld) to reduce handling stress during later training. Next, animals were trained and habituated for 3 days with head-restraint in the training setup with a running wheel. After habituation, animals were placed in a two-photon microscopy setup. Once the mice were comfortable with the setup, they performed a visual detection task.

Visual stimulation

Stimuli were presented on a gamma-corrected Dell-P2314H 23" full HD LED monitor, placed 15 cm in front of the mouse. Stimuli were made with custom-made MATLAB scripts. Receptive field size of each region of interest (ROI) was estimated by reverse correlation after presenting 3 black and 3 white squares (7.5° - size degrees) simultaneously at pseudo random locations on the screen. The stimuli were repeated for 10-15 times at each location. The duration was 0.5 s, the interstimulus was an isoluminant gray screen, duration 1.5 s, contrast: 1.0 and maximum luminance was kept to 20% of screen max (Max luminance). For visual stimulation, various stimuli were used, depending on the behavioral experiment.

Two-photon imaging

For imaging we used a NeuroLabware standard microscope (CA, USA) equipped with a Ti-sapphire laser (Mai-Tai, Spectra-physics, CA, USA). A black cloth was used to cover the objective in order to prevent light coming from the monitor to the objective. Two-photon laser scanning microscopy was performed at 910 nm and neurons were imaged using a 1 mm field of view with 16x water-immersion objective (0.8NA) with computer-optimized optics of 1.6x magnification.

Two-photon Calcium-imaging sequences were recorded in awake behaving mice and saved in a continuous binary format (sbx, NeuroLabware). The dimensions of the images were 812 by 512 pixels, with 16 bit unsigned integer pixel depth. These files are associated with a metadata file (mat, MATLAB) that defines, among other parameters, pixel dimensions, number of channels, number of sections, and number of frames recorded. All further processing was done with MATLAB (Mathworks™).

Data analysis code

The code for all data analysis procedures described below is available at Github:

(<https://github.com/Leveltlab/SpectralSegmentation>). A flowchart of the analysis pipeline is shown

in Fig. 1 and is also present in the Github repository.

ROI selection based on cross-spectral power

We developed a pipeline for ROI extraction that works as follows: First, the images are cropped to remove border artifacts before being aligned using rigid registration with NoRMCorre (<https://github.com/flatironinstitute/NoRMCorre>), a toolbox provided by the Simons Foundation (Pnevmatikakis and Giovannucci, 2017). We adapted the entry function of this toolbox in order for it to work with files in .sbx format, produced by the Neurolabware microscope that we used, and integrated it in the pipeline. After visual inspection to ascertain that the images are well aligned, the image sequences are transposed to place time in the first dimension and width * height in the second dimension (StackTranspose.m). This makes the processing of pixel traces much more efficient in the time domain. This data is saved in binary format for later use with “_Trans.dat” as extension. In addition, we also save a downsampled version of this file with “_DecTrans.dat” as extension. Downsampling was performed with “decimate” (Mathworks) to a sampling rate of ± 1 Hz. Next, it calculates the cross-spectral power of the fluorescent signal between neighboring pixels over time. To achieve this, the data is first detrended and for each half-overlapping time window (60 seconds) the data is convolved with a hamming window. Cross-spectral density functions are calculated from the discrete Fourier transforms of these pixel-trace segments for each pixel with its eight neighbors and averaged over all time windows. Additionally, the total variance is calculated for each pixel from their average auto-spectral density function. Then, the cross-spectral power functions are normalized (see formula 1) with their respective variances.

$$P_{xy}(f) = \frac{|G_{xy}(f)|^2}{V_x V_y}$$

Formula 1. *Cross-spectral power: Where $P_{xy}(f)$ is the average normalized cross-spectral power, $G_{xy}(f)$ is the cross spectral density between x and y for frequency component f , and V_x and V_y the average variance of x and y respectively.*

Finally, the normalized cross-spectral power functions of a pixel with its eight neighbors are averaged. The result is a 2D matrix representing cross-spectral power at each frequency component for all pixels. We used this to generate an image for each spectral component. This data is saved in a separate file with “_SPSIG.mat” as extension.

Cross-spectral images are generated for spectral components between 0.017 Hz to 0.5 Hz, from image sequences recorded at a sampling rate between 10 and 30 Hz (Fig. 2). Pixels within active neurons display strong cross-spectral power below 0.4 Hz whereas background neuropil is usually non correlated making neurons clearly visible in these images (Figs. 2, 3). The images for cross-spectral components between 0.017 and 0.4 Hz are therefore used to extract ROIs (spectral.m). For each cross-spectral image in the selected frequency range, a series of morphological constraints are applied to find as many non-overlapping ROIs as possible (getSpectrois.m). First, all maxima (cross-spectral peaks) in the image are detected and sorted according to magnitude. A fraction (0.25-0.4) of these peaks with the highest values are selected and sorted in decreasing order. Based on this selection, a square area of pixels (Voxel; 50x50 pixels) is sampled for each peak, centered on the peak and contours are detected using `contourc` (MATLAB) (Fig 3D). Closed contours containing the selected peak are selected and constrained by a set of criteria:

1. To avoid that multiple peaks from the same neuron are selected, the minimal distance between peaks in each ROI should be greater than a defined threshold (20 pixels).
2. To ensure that the magnitude of the peak is well above background level, the peak should be greater than (95%) of the pixel range within a voxel.
3. Given the expected size range of cell bodies, the minimum and maximum area (number of pixels) should be between 30-400 pixels (a pixel is $\pm 1.5\mu\text{m}^2$ within our field of view: $\pm 1\text{mm}$).

4. Roundedness; The relationship between the area of a contour and the length of its circumference ($4 * \pi * \text{Area} / \text{Circumference}^2$) should be greater than 0.6 (1 = completely round, 0 = any shape), These parameters can be adapted depending on the type of ROI that a user is interested in and the magnification of the images. To select cell bodies, for example, the roundedness should be greater than 0.6 and the number of pixels should be below 100 at low magnification. Because the criteria are simple and self-evident, optimal values can easily be established with some experimentation. Depending on the density of active neurons and their processes in an image sequence, contours around correlated pixels may still represent overlapping or adjacent neural elements. Therefore, the ROIs are further restrained based on the assumption that pixels in adjacent cell bodies are not highly correlated. To achieve this, all pixel traces within the original ROI are correlated with the averaged down-sampled trace of eight neighboring pixels at the original local maximum. Based on this calculation, the ROI is constrained to an area containing pixels with correlations larger than the half maximum of the total range (Fig. 3E). In principle, this is a computationally expensive approach, but it is feasible because the numbers of pixel traces in a preselected ROI are limited in number and the traces are decimated to 1Hz. For analysis and selection purposes we also saved the mean pixel R^2 of an ROI. To calculate this we averaged the squared pixel correlations within the constrained ROI.

User interface for ROI refinement

To give users control over the selected ROIs, we developed a graphical user interface to reject ROIs outside a preferred range of properties (RoiManagerGUI.m). Additionally, the user interface allows the user to manually delete or keep ROIs. In rare cases, some ROIs have areas with pixels that have low or negative correlations. This may indicate that the ROI contains signals from multiple neuronal sources, or that registration was suboptimal and the neuron was not located at the ROI during the entire recording. We therefore developed the option to split these ROIs (Fig. 7B-E). The user interface creates four reference points at the distal edges of the ROI. The fluorescence signal from these reference points is then correlated with the signal of each pixel in the ROI. This creates four

correlation values per pixel of the ROI. These are used to create a color-coded image in the user interface, indicating the location of different signal sources in the ROI. The pixels in the ROI can then be subjected to k-means clustering. After setting the number of clusters the user can decide to split such an ROI in two or more ROIs or to delete part of the ROI. The user can also add more reference points if clustering needs to be improved.

We also included the option to create new ROIs in the user interface, for example when neurons were missed by the automated analysis. These new ROIs can be added in two different ways. One option is to manually draw the contour of the ROI. The other option is to let the computer draw the ROI, based on the cross-spectral image (or any other user-defined background image, such as the fluorescent image) and a threshold set by the user (Fig. 7A).

Signal extraction and neuropil subtraction

To extract the calcium signals for each ROI (`retrievesignals.m`), all pixel traces within the ROI contours are averaged. The signals are neuropil corrected by subtracting the averaged signal of a neuropil area from the ROI signal. A donut-shaped neuropil area is created for each ROI. To achieve this, a small buffer area with a width of 2 pixels ($\sim 2 \mu\text{m}$) is first added around each ROI. The neuropil area is defined by first enlarging the ROI by 20 pixels ($\sim 20 \mu\text{m}$) using a circular filter, after which the central and adjacent ROIs and their buffer areas are excluded from this area. To prevent overcorrection, the neuropil signal is multiplied by 0.7, in accordance with previous studies (Chen et al., 2013; Khan et al., 2018; Tegtmeier et al., 2018).

Spike estimation

The extracted ROI signal can be converted into an estimate of a spike train (`DeconvolveSignals.m`) with the `MLspike` toolbox (Deneux et al., 2016), which has to be downloaded via their github (<https://github.com/MLspike>). The spike train is then saved in the same format as the regular calcium signals.

Identification of the same ROIs in chronically recorded datasets

Finally, we include a toolbox to identify the same ROIs in chronic recordings of the same brain region (ChronicMatching.m). It first registers the spectral images of the recordings to ensure that each ROI will be located at exactly the same position in all recordings. To achieve this, the spectral images are normalized so that all values were in the range from -1 to 1. Next, the registration of the spectral images is done by repeated translation and rotation. Each recording is registered to a reference recording chosen by the user. Preferentially, one of the middle recordings is used as a reference in order to minimize the difference between the reference and the recordings to be registered.

The distance over which recordings need to be translated is calculated by doing a 2D cross-correlation between the reference image and the spectral images of the other recordings. The cross-correlation is calculated with `xcorr2_fft` (Masullo, 2020), which is much faster than the MATLAB built-in cross-correlation function. After the translations are applied, the images are padded with zeros to maintain the same dimensions.

To correct the rotation, each recording is rotated using bicubic interpolation over a range of different angles, from 1° clockwise to 1° counterclockwise in steps of 0.05°. Each rotation is compared to the reference image with a 2D correlation and the best fit is applied if the correlation is at least 0.005 higher than the original image. Several rounds of translation and rotation are applied until no significant further improvement is achieved.

After registration, ROIs between all chronic recordings within an experiment are matched. A minimum percentage of overlap threshold is set. In the example presented here, we chose 67.5% based on the best balance between false positives and false negatives as determined by inspection with the chronic viewer user interface. The ROI matching is represented in a 2D matrix (the “match matrix”), consisting of a column for each recording and rows with the ROI numbers in each recording that are matched to each other. If no match for a particular ROI is found in a recording, the cell was kept blank.

To create the match matrix, the following three steps are taken:

1. For each ROI in each recording, the overlapping ROIs from all other recordings are identified. The percentage of the reference ROI that is covered by each overlapping ROI of other recordings was calculated (“overlap”) and saved as a putative match if it is above the overlap threshold.
2. Next, the overlap for each pair of putatively matched ROIs is calculated in the opposite direction (i.e. the percentage of overlapping ROI that is covered by the reference ROI). The average of the two overlap values are averaged, and putative matches whose average overlap is below the overlap threshold (in our example 67.5%) are discarded. Calculating the overlap in these two simple steps automatically takes many parameters of the neurons into account: if the sizes, shapes or positions of two ROIs differ significantly the overlap value will always be small.
3. To obtain the final matching matrix, the data needs to be merged in order to match the same ROIs in all recordings, not just in pairs of recordings. The merging process includes ‘mutual linking’: if an ROI from recording A is matched only to recording B, but that ROI from recording B has matches to A and C, it is implied that the ROI from recording A is also matched to the ROI in recording C. This mutual linking increases the number of matched ROIs.

The results can be checked in a user interface (ChronicViewer.m). The matches can be verified by selecting a cell in the match matrix, which will light up the ROI contours of the match. Clicking on ROIs in the main image will show the ROI numbers and match information in a table. The match matrix can be edited if necessary.

References

- Apthorpe NJ, Riordan AJ, Aguilar RE, Homann J, Gu Y, Tank DW, Seung HS. 2016. Automatic neuron detection in calcium imaging data using convolutional networks. *Adv Neural Inf Process Syst* 3278–3286.
- Chen TW, Wardill TJ, Sun Y, Pulver SR, Renninger SL, Baohan A, Schreiter ER, Kerr RA, Orger MB, Jayaraman V, Looger LL, Svoboda K, Kim DS. 2013. Ultrasensitive fluorescent proteins for imaging neuronal activity. *Nature* **499**:295–300. doi:10.1038/nature12354
- Cichon J, Gan WB. 2015. Branch-specific dendritic Ca²⁺ spikes cause persistent synaptic plasticity. *Nature* **520**:180–185. doi:10.1038/nature14251
- Dana H, Sun Y, Mohar B, Hulse BK, Kerlin AM, Hasseman JP, Tsegaye G, Tsang A, Wong A, Patel R, Macklin JJ, Chen Y, Konnerth A, Jayaraman V, Looger LL, Schreiter ER, Svoboda K, Kim DS. 2019. High-performance calcium sensors for imaging activity in neuronal populations and microcompartments. *Nat Methods* **16**:649–657. doi:10.1038/s41592-019-0435-6
- Deneux T, Kaszas A, Szalay G, Katona G, Lakner T, Grinvald A, Rozsa B, Vanzetta I. 2016. Accurate spike estimation from noisy calcium signals for ultrafast three-dimensional imaging of large neuronal populations in vivo. *Nat Commun* **7**. doi:10.1038/ncomms12190
- Driscoll LN, Pettit NL, Minderer M, Chettih SN, Harvey CD. 2017. Dynamic Reorganization of Neuronal Activity Patterns in Parietal Cortex. *Cell* **170**:986-999.e16. doi:10.1016/j.cell.2017.07.021
- Engert F, Bonhoeffer T. 1999. Dendritic spine changes associated with hippocampal long-term synaptic plasticity. *Nature* **399**:66–70. doi:10.1038/19978
- Gambino F, Pagès S, Kehayas V, Baptista D, Tatti R, Carleton A, Holtmaat A. 2014. Sensory-evoked LTP driven by dendritic plateau potentials in vivo. *Nature* **515**:116–119. doi:10.1038/nature13664
- Giovannucci A, Friedrich J, Gunn P, Kalfon J, Brown BL, Koay SA, Taxidis J, Najafi F, Gauthier JL, Zhou

- P, Khakh BS, Tank DW, Chklovskii DB, Pnevmatikakis EA. 2019. CalmAn an open source tool for scalable calcium imaging data analysis. *Elife* **8**. doi:10.7554/eLife.38173
- Iacaruso MF, Gasler IT, Hofer SB. 2017. Synaptic organization of visual space in primary visual cortex. *Nature* **547**:449–452. doi:10.1038/nature23019
- Jia H, Rochefort NL, Chen X, Konnerth A. 2010. Dendritic organization of sensory input to cortical neurons in vivo. *Nature* **464**:1307–1312. doi:10.1038/nature08947
- Kaifosh P, Zaremba JD, Danielson NB, Losonczy A. 2014. SIMA: Python software for analysis of dynamic fluorescence imaging data. *Front Neuroinform* **8**:80. doi:10.3389/fninf.2014.00080
- Khan AG, Poort J, Chadwick A, Blot A, Sahani M, Mrsic-Flogel TD, Hofer SB. 2018. Distinct learning-induced changes in stimulus selectivity and interactions of GABAergic interneuron classes in visual cortex. *Nat Neurosci* **21**:851–859. doi:10.1038/s41593-018-0143-z
- Klibisz A, Rose D, Eicholtz M, Blundon J, Zakharenko S. 2017. Fast, simple calcium imaging segmentation with fully convolutional networks. *Lecture Notes in Computer Science (Including Subseries Lecture Notes in Artificial Intelligence and Lecture Notes in Bioinformatics)*. Springer Verlag. pp. 285–293. doi:10.1007/978-3-319-67558-9_33
- Mank M, Santos AF, Drenth S, Mrsic-Flogel TD, Hofer SB, Stein V, Hendel T, Reiff DF, Levelt C, Borst A, Bonhoeffer T, Hübener M, Griesbeck O. 2008. A genetically encoded calcium indicator for chronic in vivo two-photon imaging. *Nat Methods* **5**:805–811. doi:10.1038/nmeth.1243
- Maruyama R, Maeda K, Moroda H, Kato I, Inoue M, Miyakawa H, Aonishi T. 2014. Detecting cells using non-negative matrix factorization on calcium imaging data. *Neural Netw* **55**:11–9. doi:10.1016/j.neunet.2014.03.007
- Masullo A. 2020. `xcorr2_fft(a,b)` - File Exchange - MATLAB Central. https://www.mathworks.com/matlabcentral/fileexchange/53570-xcorr2_fft-a-b
- Mukamel EA, Nimmerjahn A, Schnitzer MJ. 2009. Mukamel et al 2009 Automated Analysis of Cellular signals from calcium imaging data. *Supp Data* 1–32. doi:10.1016/j.neuron.2009.08.009
- Pachitariu M, Stringer C, Dipoppa M, Schröder S, Rossi LF, Dalgleish H, Carandini M, Harris KD. 2017.

Suite2p: beyond 10,000 neurons with standard two-photon microscopy. *bioRxiv* 061507.

doi:10.1101/061507

Petersen A, Simon N, Witten D. 2018. SCALPEL: EXTRACTING NEURONS FROM CALCIUM IMAGING

DATA. *Ann Appl Stat* **12**:2430–2456. doi:10.1214/18-AOAS1159

Petreaun L, Mao T, Sternson SM, Svoboda K. 2009. The subcellular organization of neocortical

excitatory connections. *Nature* **457**:1142–1145. doi:10.1038/nature07709

Pnevmatikakis EA, Giovannucci A. 2017. NoRMCorre: An online algorithm for piecewise rigid motion

correction of calcium imaging data. *J Neurosci Methods* **291**:83–94.

doi:10.1016/j.jneumeth.2017.07.031

Pnevmatikakis EA, Soudry D, Gao Y, Machado TA, Merel J, Pfau D, Reardon T, Mu Y, Lacefield C, Yang

W, Ahrens M, Bruno R, Jessell TM, Peterka DS, Yuste R, Paninski L. 2016. Simultaneous

Denoising, Deconvolution, and Demixing of Calcium Imaging Data. *Neuron* **89**:285–99.

doi:10.1016/j.neuron.2015.11.037

Reynolds S, Abrahamsson T, Schuck R, Jesper Sjöström P, Schultz SR, Dragotti PL. 2017. Able: An

activity-based level set segmentation algorithm for two-photon calcium imaging data. *eNeuro*

4. doi:10.1523/ENEURO.0012-17.2017

Smith SL, Häusser M. 2010. Parallel processing of visual space by neighboring neurons in mouse

visual cortex. *Nat Neurosci* **13**:1144–9. doi:10.1038/nn.2620

Spaen Q, Asín-Achá R, Chettih SN, Minderer M, Harvey C, Hochbaum DS. 2019. HNCcorr: A Novel

Combinatorial Approach for Cell Identification in Calcium-Imaging Movies. *eNeuro* **6**.

doi:10.1523/ENEURO.0304-18.2019

Svoboda K, Tank DW, Denk W. 1996. Direct measurement of coupling between dendritic spines and

shafts. *Science (80-)* **272**:716–719. doi:10.1126/science.272.5262.716

Szalay G, Judák L, Katona G, Ócsai K, Juhász G, Veress M, Szadai Z, Fehér A, Tompa T, Chiovini B,

Maák P, Rózsa B. 2016. Fast 3D Imaging of Spine, Dendritic, and Neuronal Assemblies in

Behaving Animals. *Neuron* **92**:723–738. doi:10.1016/j.neuron.2016.10.002

Tegtmeier J, Brosch M, Janitzky K, Heinze H-J, Ohl FW, Lippert MT. 2018. CAVE: An Open-Source Tool for Combined Analysis of Head-Mounted Calcium Imaging and Behavior in MATLAB. *Front Neurosci* **12**. doi:10.3389/fnins.2018.00958

Wilson DE, Whitney DE, Scholl B, Fitzpatrick D. 2016. Orientation selectivity and the functional clustering of synaptic inputs in primary visual cortex. *Nat Neurosci* **19**:1003–1009. doi:10.1038/nn.4323

Winnubst J, Cheyne JE, Niculescu D, Lohmann C. 2015. Spontaneous Activity Drives Local Synaptic Plasticity In Vivo. *Neuron* **87**:399–410. doi:10.1016/j.neuron.2015.06.029

Zhou P, Resendez SL, Rodriguez-Romaguera J, Jimenez JC, Neufeld SQ, Giovannucci A, Friedrich J, Pnevmatikakis EA, Stuber GD, Hen R, Kheirbek MA, Sabatini BL, Kass RE, Paninski L. 2018. Efficient and accurate extraction of in vivo calcium signals from microendoscopic video data. *Elife* **7**. doi:10.7554/eLife.28728